Springback in assembly of mirror panels with stamped supports for concentrating solar power applications

Johannes Pottas[1*], Joe Coventry[1*]

[1] Research School of Electrical, Energy and Materials Engineering, Australian National University, Canberra, Australia

* Corresponding authors: johannes.pottas@anu.edu.au, joe.coventry@anu.edu.au

1 Introduction

Solar collector fields consisting of a large number of heliostats are used to reflect and concentrate sunlight onto a tower receiver (Figure 1a) in concentrating solar power (CSP) plants. In the most common tower CSP configuration, shown in Figure 1b, the concentrated light is used to heat a recirculating molten salt heat transfer fluid. A portion of this flow is used to generate steam immediately to drive a Rankine power cycle, while the remainder is stored in insulated tanks to enable 24 hour dispatchable power generation.

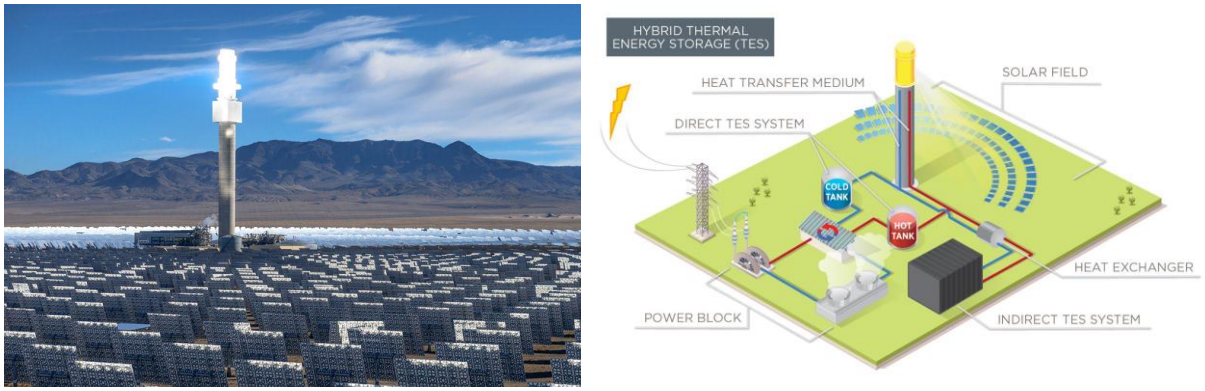

(a) (b)

Fig.1: (a) A view of the heliostat field and receiver tower at the 110 MW Crescent Dunes plant [2] and (b) a schematic of a typical CSP tower plant with thermal energy storage [1].

The solar collector field accounts for 25% to 40% of the direct capital cost of a CSP plant [1] and remains a focus area for several government funded cost reduction initiatives around the world. Heliostat costs have almost halved over the past 5-10 years due to increased commercial deployment, and are presently estimated to be as low as 100 USD/m^2 [**Error! Reference source not found.**]. However, for CSP to be a competitive renewable energy supply option into the future, heliostat costs are likely to need to halve again in the coming decade [**Error! Reference source not found.**]. Two mirror panel configurations are commonly used in CSP tower plants, namely stamped panels and sandwich panels. Stamped panel technology is currently more widespread due to its readiness for high volume manufacture and its low cost. Further cost reductions can be achieved by developing optimised stamped supports and improved assembly processes.

Final assembly of heliostat mirror facets is often done on a mould to impart the desired curvature. However, springback from the mould due to elastic strain recovery can cause unwanted shape deformations. This study investigates the effect of springback for a mirror facet with a stamped support using LS-Dyna to simulate the assembly process. The predicted shape is compared to prototype mirrors measured photogrammetrically. The optical qualities of the final measured and simulated shapes are analysed using Monte Carlo ray tracing.

2 Prototype details

The prototypes are fabricated using incrementally formed (IF) back-structures as a proxy for the stampings, and two different reflective structures are tested – a glass-on-metal laminate (GOML)

formed from a 1 mm glass mirror and 0.4 mm steel backing, and a single 3mm glass mirror. The structures are referred to as prototype 1 and 2, respectively in subsequent sections.

2.1 Incremental forming

The support was incrementally formed from 0.4 mm Zincalume ZnAl alloy-coated steel using a conventional CNC router, shown in Figure 2a, with a 10 mm hemispherical forming tool. A negative die made of medium density fibre board was used to support the sheet during forming. Manual measurements of support distortion after forming were made by placing the support on a flat table and recording the height difference at the points indicated by the red dots in Figure 2b. The flange angles relative to the flat surface were estimated at the same locations. The angles of the support top surface in the circled regions below were also estimated.

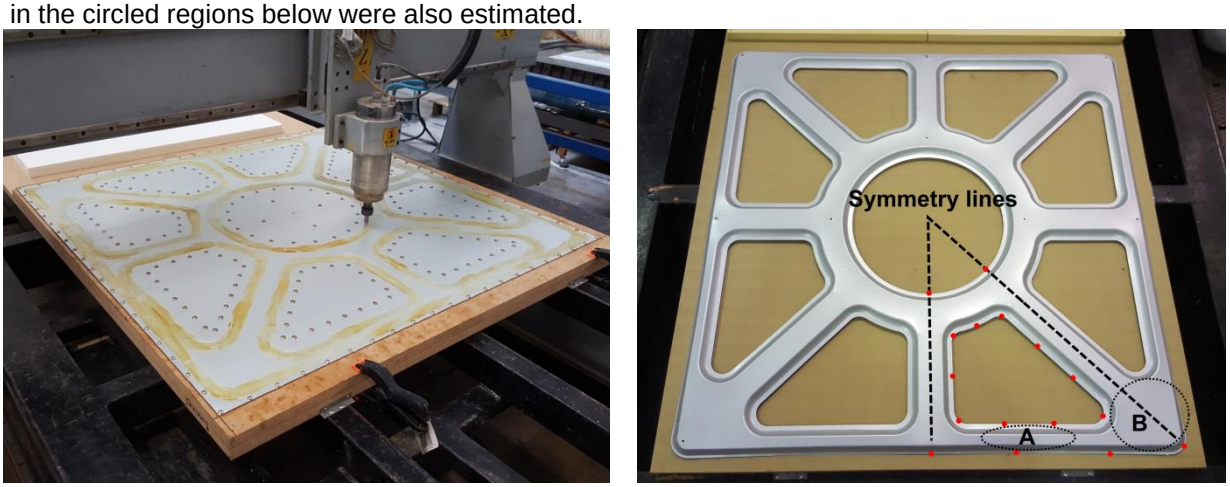

(a) (b)

Fig.2: (a) Incremental forming of the 0.4 mm sheet using a CNC router and (b) the final incrementally formed support showing the points where distortions were measured.

2.2 Panel assembly process

The support and facing materials are elastically deformed by a vacuum bag (Figure 3a) over a mould surface with a 31.3 m spherical radius of curvature (ROC) and glue bonded to form a curved panel. A negative die made from expanded polystyrene (Figure 3b) is used between the vacuum bag and the panel materials in an attempt to focus the force on the flanges of the support where it is bonded to the facing material. The vacuum is released after curing and the panel springs back slightly to maintain a near-spherical surface curvature.

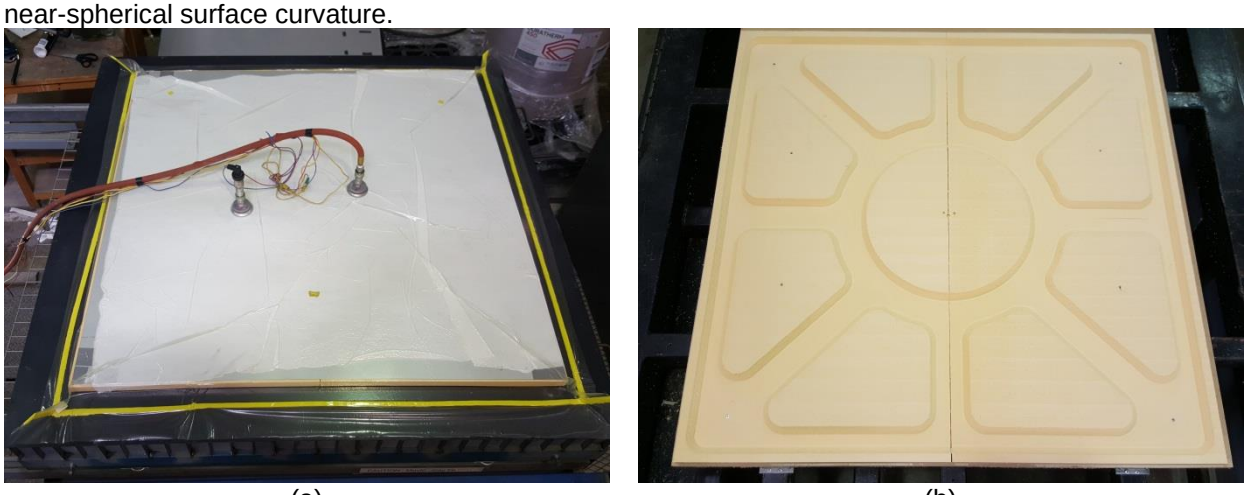

(a) (b)

Fig.3: (a) The vacuum bag assembly process and (b) the foam die used to focus the vacuum force on the support flanges during assembly.

2.3 Photogrammetric measurements

Close-range photogrammetry is a non-contact 3D measurement technique which can be used to reconstruct an object from photographs. The method can yield 3D length measurement errors in the range 0.2–1 µm, although more typically 10–15 µm, where error is defined as the difference between a measured length and a calibrated reference length [5].

The surface curvatures of the prototypes were measured photogrammetrically from sets of 27 images with 1824 projected dots. An example of a photogrammetry image and the resulting 3D point cloud are shown in Figure 4.

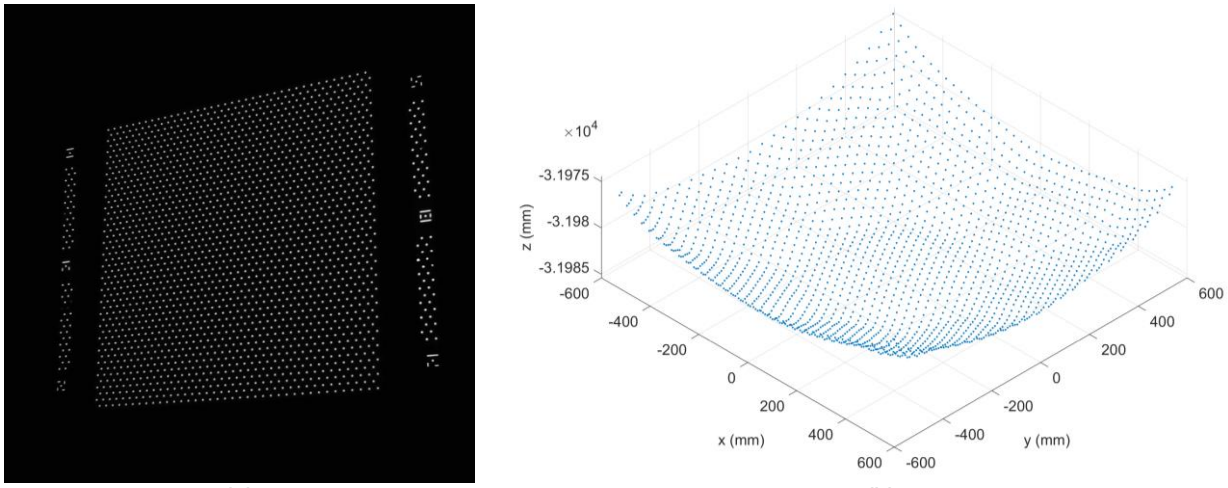

(a) (b)

Fig.4: (a) One of a set of 27 images used to characterise the shape of prototype 1 and (b) a 3D scatter plot of the resulting measurement points.

3 Model details

A finite element model was built to simulate the assembly process. Each component (support, steel sheet, glass sheet and mould) was modelled as a separate mesh as shown in Figure 5. In the first contact phase, the meshes were allowed to slide over one another. The mould was fully constrained and three nodal set loads, representing the vacuum force, were applied to push the components onto the mould surface. Once the force was fully applied, the mirror panel contacts were switched to tied contacts to represent the glue bond. The force was reduced until it was fully removed so that the combined structure sprung back to its final shape.

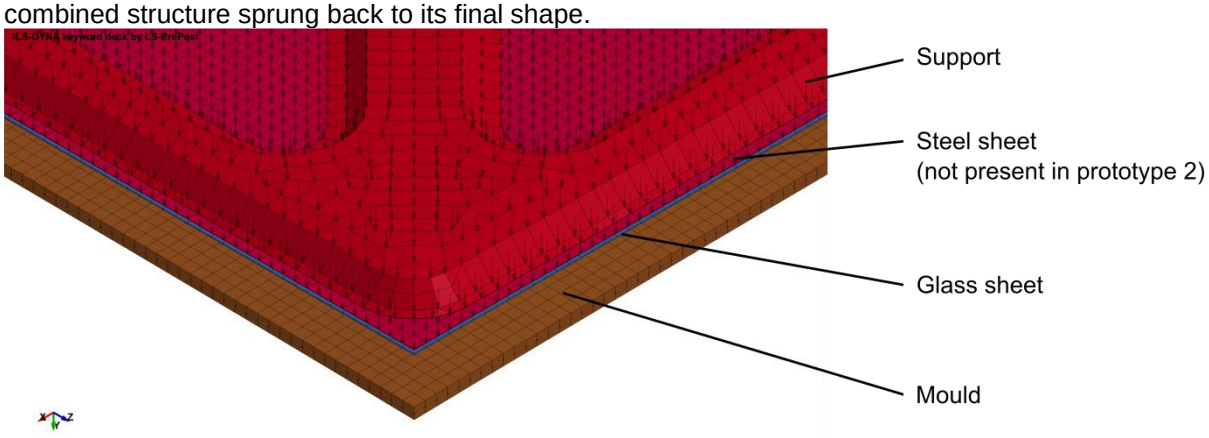

Fig.5: The model of prototype 1 consisting of 4 disjoint meshes.

The simulations described in the paper are numbered, with each number representing a separate case study that may have different modelling parameters, settings and part geometries. The remainder of this section provides details of shared model characteristics as well as specific details of selected models.

3.1 Geometry model

A CAD model of the support geometry was imported to LS-Prepost. This geometry did not include any of the recorded distortions and represented the idealised geometry of the support without distortions.

3.2 Mesh, constraints and loads

The support mesh was created from the imported CAD geometry. The support mesh consists primarily of quadrilateral shell elements with 15 mm nominal size, with a small fraction of triangular shells where they could not be avoided. Simulation #1 used the undistorted geometry. It was found that the flanges in the incrementally formed support were not flat, and that springback in the forming process resulted in distortions of 3 mm to 10 mm from the desired shape. Therefore, in simulation #2 the mesh was updated with these distortions (Update 1 in Table 3), based on manual measurements. It was further observed that there was an overall pre-curvature following the incremental forming, as can be seen comparing Figures 6a and 6b. Initially this was thought not to be important, as only a small load is required to deform the support to the mould. However, as the results of simulation #3 show, the initial precurvature does influence the final curvature of the mirror after bonding. Simulations 3# to #5 used a mesh with updated distortions including this precurvature (Update 2 in Table 3).

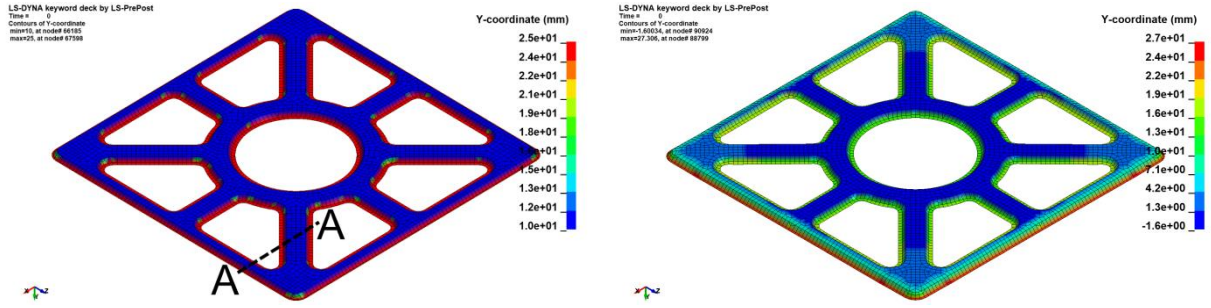

(a) (b)

Fig.6: Fringes of y-coordinate at 0 ms to show the (a) undistorted mesh used in simulation #1 and (b) the distorted mesh in simulation #3 based on manually measured distortions. The cross section A-A in (a) is referred to later in Fig. 15.

The meshes of the sheet components (the steel and glass sheets) were created parametrically in LS-Prepost. The mould geometry was created parametrically and meshed in LS-Prepost. The sheet and mould meshes consisted of only quadrilateral elements with a size of 10 mm. The vacuum force was represented by 3 separate node set loads shown in Figure 7 so that the distribution of force on different parts of the model could be adjusted.

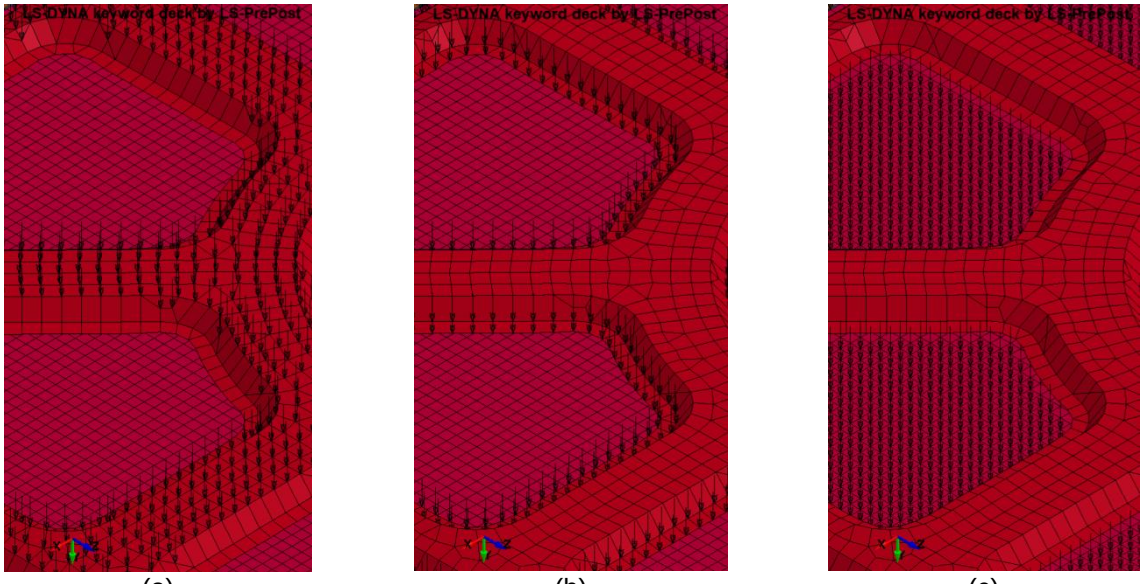

(a) (b) (c)

Fig.7: Separate unequal loads applied to (a) the top of the support, (b) the support flanges and (c) the regions of sheet between the flanges.

Two approaches were tested to constrain the mould. Initially, the mould was simulated as being rigid and fully constrained in translation and rotation. Due to early problems with negative contact energies and unrealistically high contact forces, the mould was later modelled as an elastic material with each node fully constrained. This improved the contact energy issue but did not resolve it.

3.3 Contact

Several combinations of contact algorithms were tested in an attempt to avoid distortions and instability caused by unphysical contact forces. The successful configuration consisted of the combination of contacts shown in Table 1. Each contact had a birth and death time which is shown graphically in Figure 8.

Contact ID	Slave	Master	Type	Birth/death
3	Glass sheet	Mould	***AUTOMATIC_SURFACE_TO_SURFACE**	
6	Glass sheet	Steel sheet	***AUTOMATIC_SURFACE_TO_SURFACE**	DT = 301 ms
2	Steel sheet	Support	***AUTOMATIC_SURFACE_TO_SURFACE_MORTAR**	DT = 301 ms
5	Glass sheet	Steel sheet	***TIED_SHELL_EDGE_TO_SURFACE_BEAM_OFFSET**	BT = 300 ms
4	Support	Steel sheet	***TIED_SHELL_EDGE_TO_SURFACE_BEAM_OFFSET**	BT = 300

Table 1: Keyword types used for the various contact interfaces.

The load scale factor is ramped from 0 to 1 and contacts are switched from untied to tied according to Fig. 8.

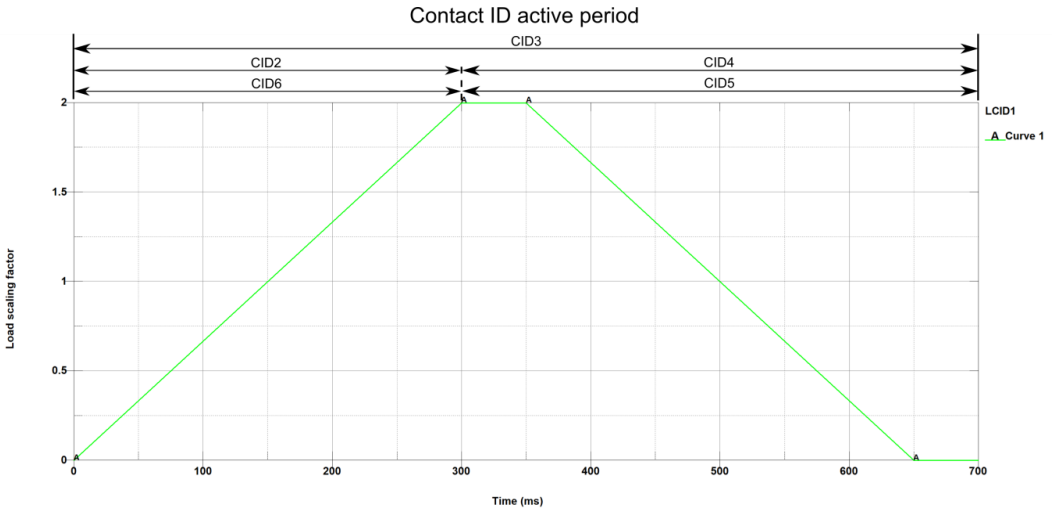

Fig.8: Graph of load scaling factor vs. time showing the active periods of each contact interface.

3.4 Material models and other settings

The glass and steel materials were modelled using ***MAT_ELASTIC** and ***MAT_PIECEWISE_LINEAR_PLASTICITY**, respectively. Other pertinent settings are noted in Table 2.

Card	Setting	Value	Comments
CONTROL_ACCURACY	INN	4	
CONTROL_CONTACT	IGNORE	1	
CONTROL_ENERGY	HGEN,RWEN, SLNTEN,RYLEN	2,2,1,1	Also tried 1,1,1,1 with change in accuracy.
DAMPING_GLOBAL	VALDMP	0.1	
DAMPING_PART_STIFFNESS_SET	COEFF	0.1	All parts included
SECTION_SHELL	SHRF	5/6	Also tested 0 and 1 with negligible effect on accuracy.

Table 2: Other simulation control settings.

4 Method

The following procedure was followed for each of the measured and predicted surface curvatures.

4.1 Data preparation

A sphere was fitted to the surface points in Matlab. The data set was transformed so that it is concave upward, centered at the origin, and so that one edge is aligned with the x-axis.

The FEA surfaces were defined by 12321 points whereas the photogrammetric measurements consisted of only 1824 points. The FEA surfaces were coarsened retrospectively by mapping their z-coordinates (interpolated linearly) to the (x,y) coordinates of the photogrammetry measurements. An example of the original and coarsened version of an FEA surface is shown in Figure 9. This was done so that subsequent slope error calculations for the measured and predicted surfaces would be done using points with similar spacing. Data spacing is known to affect slope error statistics.

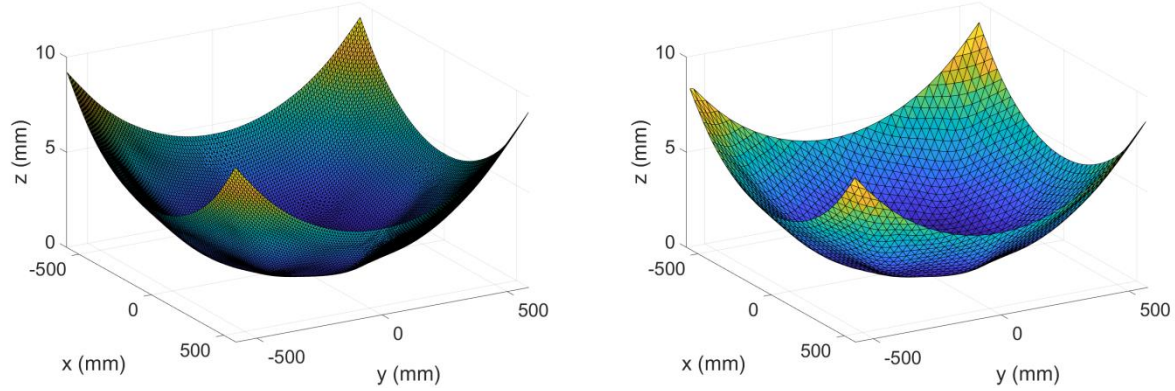

Fig.9: An example of (a) a triangulated mirror surface from simulation output and (b) the same surface coarsened to match the spacing of photogrammetry measurements.

4.2 Z-height error calculations

The z-coordinates of the surface points were subtracted from the z-coordinates of the fitted sphere so that a map of z-error was produced. The z-error surface was triangulated and plotted for qualitative comparison, and the radius of curvature was stored for comparison between sets.

4.3 Slope error calculations

The surface points were triangulated and their face normal directions were compared to the ideal normal directions at the corresponding locations on the spherical surface — a measure known as slope error. Slope error maps were produced and the root-mean-square (RMS) error was calculated.

4.4 Ray tracing

Ray tracing was carried out using the mirror surfaces to obtain a flux map and peak flux concentration ratio. The triangulated surfaces were exported from Matlab in .stl format and imported to Tonatiuh — an open source Monte Carlo ray tracing code for CSP applications [6]. The ray tracing model shown in Figure 10 consisted of the sun as a light source at 20° elevation, the .stl mirror surface at 10° elevation and the target surface at 0° elevation. Solar radiation was modelled as the Buie sunshape [7] with 2% circumsolar ratio and 1 kW/m^2 direct normal irradiance. The mirror surface was modelled as being perfectly specular and having a reflectance of 95%.

The focal distance of a spherical reflector [8] is given by:

$$f = \frac{r}{2} cos\mu \qquad [1]$$

where r is the radius of curvature and μ is the angle between the reflector axis and the incident rays. Since $cos\mu = 0.999$ in this case, the target is placed at a distance $\frac{r}{2}$ from the reflector.

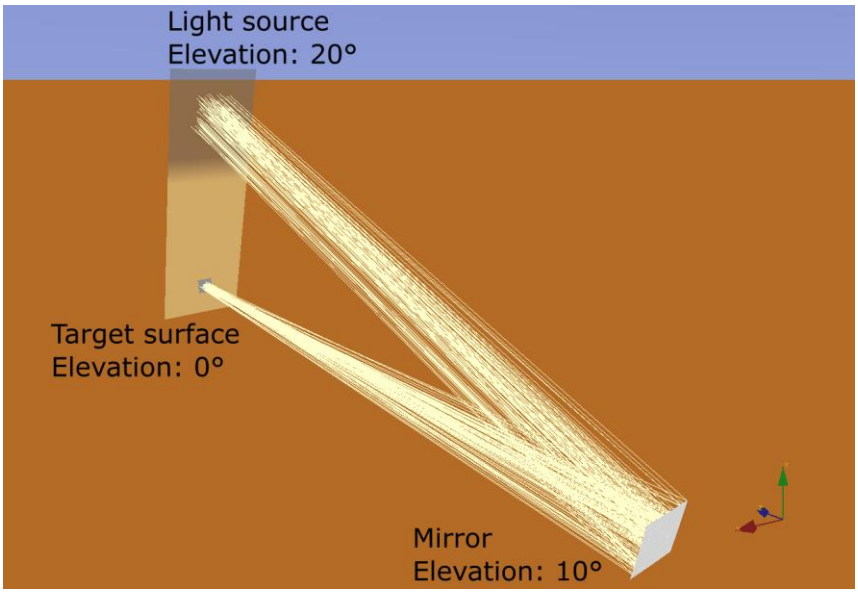

Fig.10: A visualisation of the Monte Carlo ray tracing model in Tonatiuh.

5 Results

The shape analyses of the measured and simulated surface curvatures are presented here. Note that the evolution of the simulation method yielding these results is described below in Section 6. Section 5.1 provides a summary of the results of each of the experimental and simulated curvatures in Table 3. Section 5.2 contains a comparison of the z-error maps of the experimental surfaces to the best-matching simulated surfaces. Other interesting z-error maps are given in Section 5.3 to provide context for some of the discussion points on modelling methodology which follow in section 6.

5.1 Summary of shape analysis results

Prototype	Experiment or simulation	Mesh distortion	Support top force (Fig.7:(a))	RMS slope error (mrad)	Max. negative z-error (mm)	Max. positive z-error (mm)	ROC (m)	Peak concentration ratio	Figure number
1	Experiment	-	Normal	7.5	-1.6	1.5	32.0	12.0	11a
2	Experiment	-	Normal	2.7	-0.3	0.5	41.7	22.5	11b
1	Simulation #3	Update 2	Normal	7.3	-1.7	0.7	37.6	6.8	11c
2	Simulation #5	Update 2	Normal	2.8	-0.9	0.4	38.7	28.1	11d
1	Simulation #2	Update 1	Normal	2.6	-0.7	0.3	38.9	26.6	11e
1	Simulation #1	No	Normal	1.6	-0.2	0.2	38.9	45.8	12a
1	Simulation #4	Update 2	High	6.1	-1.5	0.8	32.2	9.0	12b

Table 3: Summary of shape analyses of the experimental and simulated surfaces.

5.2 Comparison of experimental and simulated error maps

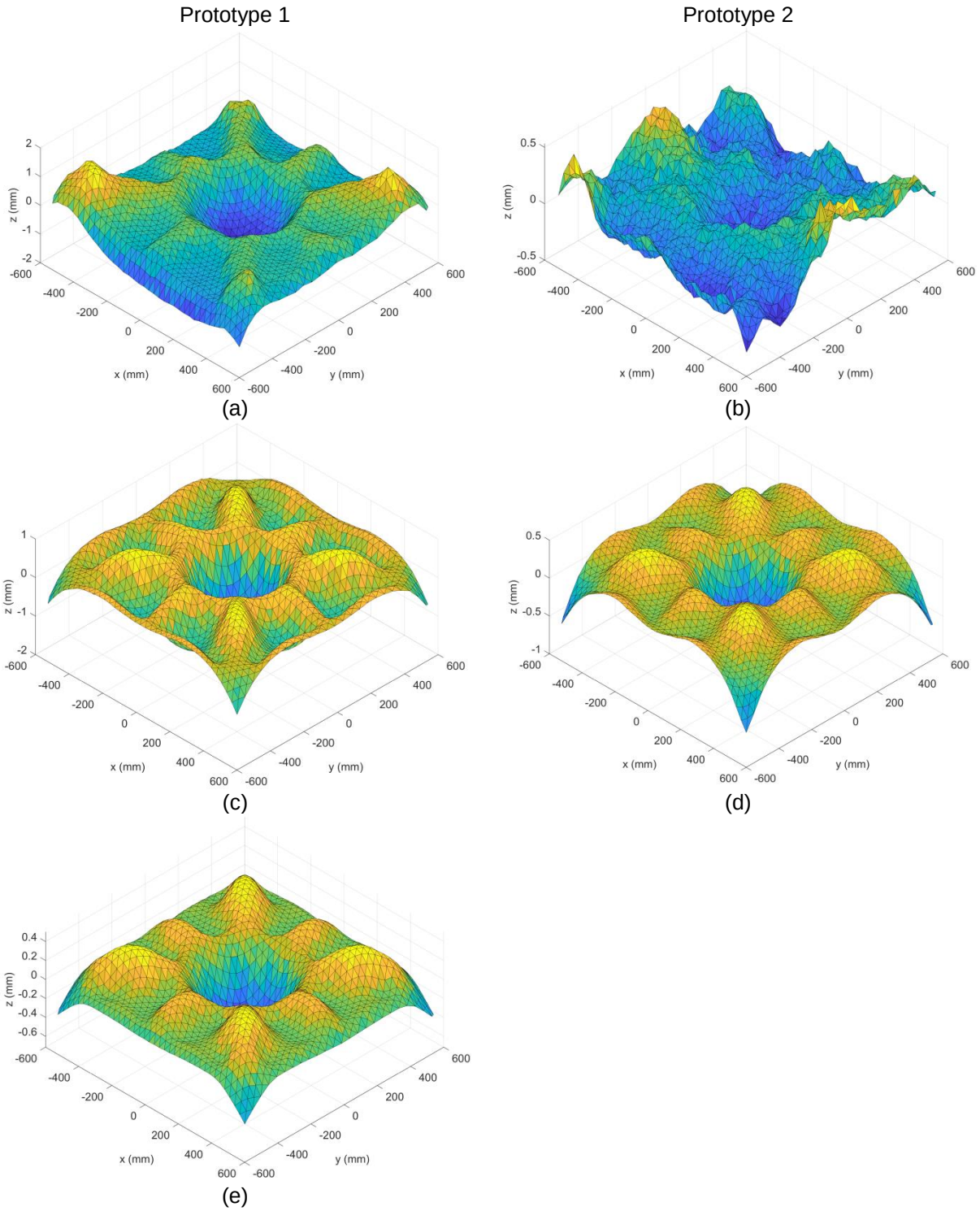

Fig.11: The z-error maps of experimental and simulated surfaces corresponding to the results in Table 3. Figures on the left hand side are Prototype 1 (reflective surface is the GOML structure) and figures on the right hand side are Prototype 2 (reflective surface is the 3mm glass mirror). The top row (a) and (b) shows the measured experimental z-error maps. The middle row (c) and (d) shows the best fit z-error map resulting from the simulation after updating the support to include distortions in the flanges plus some initial pre-curvature (Update 2). The bottom row (e) shows the result of the simulation including distortion of the support in the region of the flanges, but neglecting the observed pre-curvature (Update 1).

5.3 Other error maps

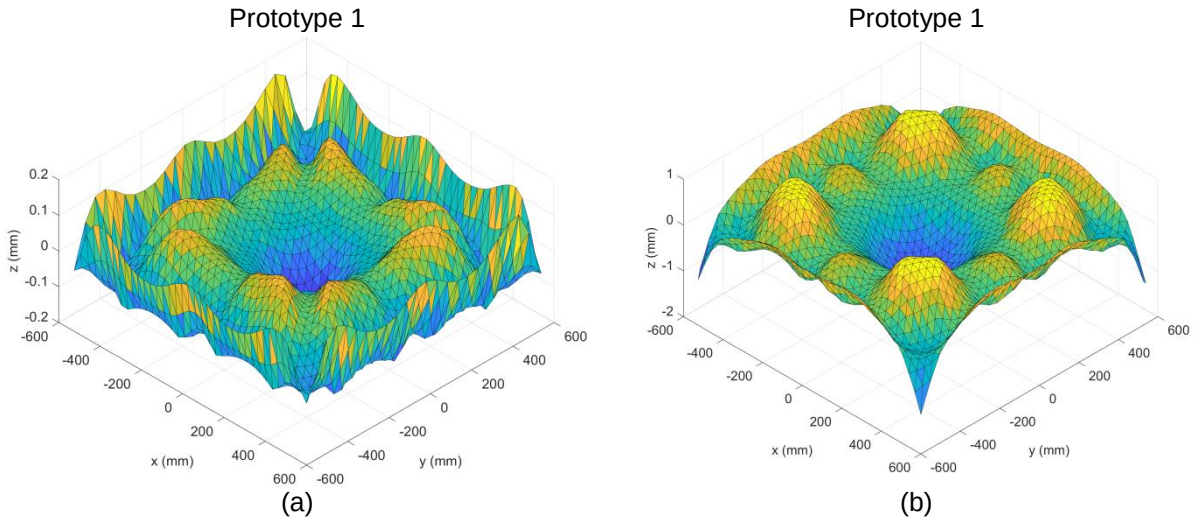

Fig.12: The z-error maps of (a) simulation #1 and (b) simulation #4, both for Prototype 1 where the reflective surface is the GOML structure.

6 Discussion

6.1 Negative contact energy

Contact algorithm-related distortions and accelerations plagued early attempts to model this problem accurately. Several combinations of automatic and conventional penalty- and constraint-based algorithms were tested without success. The undesired contact behavior was characterised by large contact forces developing during the load increase or reduction phases — in some cases far greater than the applied loads, and often unbalanced, resulting in the sum of slave and master (SoSM) energy being negative and large in magnitude. This behavior typically caused premature termination due to out-of-range nodal velocities. An example of erratic contact interface forces and the resulting distortions are shown in Figure 13. In this instance, the simulation progressed normally until contact instability initiated around 437 ms. The problematic contacts in this simulation were ***TIED_SURFACE_TO_SURFACE_OFFSET.** The issue was resolved by switching to ***AUTOMATIC_SURFACE_TO_SURFACE_MORTAR** contact for the untied phase and ***TIED_SHELL_EDGE_TO_SURFACE_BEAM_OFFSET** for the tied phase.

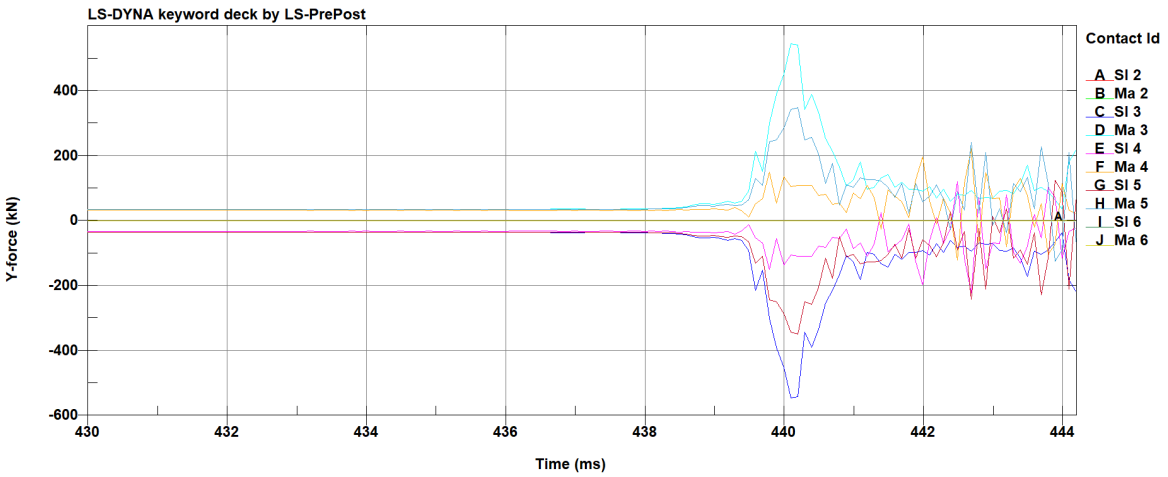

Fig.13: An example of erratic contact forces resulting in unwanted distortions and accelerations, and premature termination.

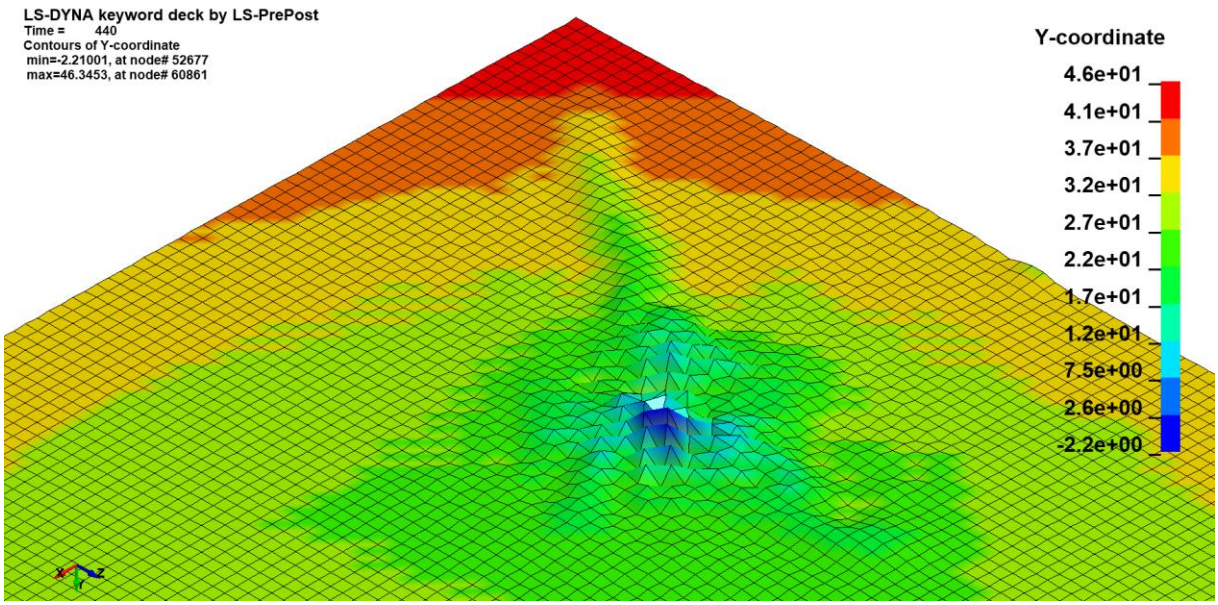

Fig.14: Distortions of the front mirror surface caused by the non-physical contact forces shown in Figure 13.

6.2 The role of force distribution on ROC and slope error prediction

A comparison of the shape statistics of the measured and simulated curvatures of prototype 1 in Table 3 shows that the model is able to predict either slope error or ROC accurately using different load distributions. For prototype 1, simulation #3 predicts slope error accurately, but overpredicts ROC by 5.6 m. Simulation #4, on the other hand, predicts the correct ROC, but underpredicts slope error by 1.4 mrad. A similar trend is seen for prototype 2, where simulation #5 is able to predict slope error within 0.1 mrad of the experimental value, but underpredicts ROC by 3 m.

The models used in simulations #3 and #4 are identical except for the force distributions on the flanges and top of the support shown in Figure 7a and 7b, respectively. The force on the top of the support is three times higher in simulation #4 than in #3, causing the flanges to slide further apart during the first contact phase before they are tied to the sheet. This behaviour results in less springback which can be seen in the lower ROC and error (both z- and slope).The total vacuum force in the experiment is known, but the forces are unevenly distributed due to the varying thickness of the foam die, and varying gap widths between the die and the support. Due to the sensitivity of the results to this distribution it is clear that this should be measured to improve the accuracy of future simulations.

6.3 Mirror panel optical performance

The purpose of this model is to predict the residual shape errors of the mirror panels after moulding, rather than to determine the performance of an individual design. However, some of the simulations are interesting to examine in terms of performance, as they provide insight into potential improvements in the manufacturing method to produce better mirror panels.

All of the results presented were produced by models using distorted support geometries (Figure 15a), except simulation #1 which was modelled according to the ideal support geometry (Figure 15b). The distortions were attempts to recreate the distortions which were manually measured on the incrementally formed support before moulding. It was necessary to model these distortions to predict the ROC and slope error correctly. However, simulation #1 shows that slope error can potentially be reduced by as much as 5.7 mrad (from 7.3 mrad in #3 to 1.6 mrad in #1) if distortions in the incrementally formed support can be minimised.

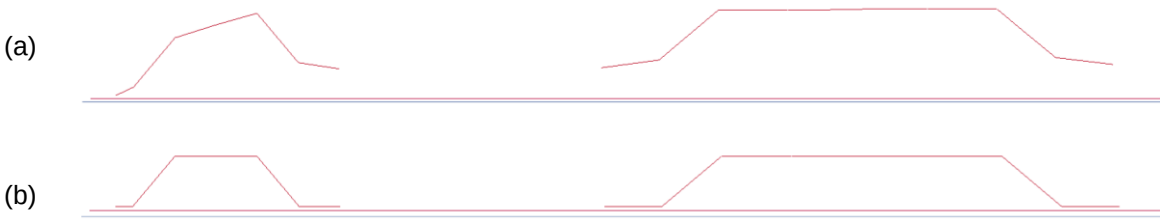

Fig.15: A cross-section at A-A in Figure 6 of the (a) distorted geometry used in simulations #3 to #5 and (b) the undistorted geometry used in simulation #1.

7 Summary

The final model setup, which is described in section 3, was able to reliably predict either slope error or ROC accurately depending on the distribution of load amongst the three nodal load sets. Since the total force applied in the experiment is known but the distribution of force is unknown, several combinations were tested. It was found that if a larger component of the force was applied to the top of the support, then ROC could be predicted accurately. If this component was reduced, then slope error was accurately predicted and the error map better resembled the experiment.

The most significant source of inaccuracy was incorrect mesh geometry. Initial simulations which used an idealised model and did not consider the distortions in the support were unable to predict the ROC, slope error or error distribution correctly. Manual measurements were made of the distortions before the panels were assembled. Due to the discovered importance of a highly accurate geometry model, future support prototypes will be measured photogrammetrically or with a coordinate measurement system.

Overall, this work has shown that apparently complex mirror shape distortions can be accurately predicted using FEA modelling of the manufacturing process, if the initial shape of the supporting structure is known. The results also indicate a positive outlook for the optical accuracy of stamped mirror panels, if distortions in the stamped support sheets can be minimised.

8 Acknowledgements

This work was funded by the Australian Renewable Energy Agency through the Australian Solar Thermal Research Institute (ASTRI). Simulations were done using computational resources and software licenses of the National Computational Infrastructure through the FB74 high performance computing grant. The authors would like to thank Satish Pathy at LSTC Technical Support for advice on contact algorithm setup.

9 Literature

[1] U.S. Department of Energy, Office of Energy Efficiency and Renewable Energy: "Solar Energy Technologies Office Fiscal Year 2019 Funding Program", DE-FOA-0002064, pp. 39

[2] SolarReserve, 2019, accessed on 13 March 2019, https://www.solarreserve.com/en/global-projects/csp/crescent-dunes

[5] Luhmann T, Robson S, Kyle S and Harley I: “Close Range Photogrammetry: Principles, Techniques and Applications”, Chap. 7, (Whittles, 2006)

[3] Pfahl A, Coventry J, Röger M, Wolfertstetter F, Vásquez-Arango JF, Gross F, Arjomandi M, Schwarzbözl P, Geiger M, Liedke P: "Progress in heliostat development", Solar Energy, 2017, 152,pp. 3-7

[4] Murphy C, Sun Y, Cole WJ, Maclaurin GJ, Mehos MS, Turchi CS: "The Potential Role of Concentrating Solar Power within the Context of DOE's 2030 Solar Cost Targets", National Renewable Energy Lab (NREL), 2019

[6] Blanco MJ, Amieva JM, Mancillas A: “The Tonatiuh Software Development Project: An open source approach to the simulation of solar concentrating systems“, in proceedings of ASME 2005 International Mechanical Engineering Congress and Exposition, pp. 157-164

[7] Buie D, Monger AG, Dey CJ: “Sunshape distributions for terrestrial solar simulations“, Solar energy, 74(2), 2003, pp. 113-22

[8] Rabl, A: “ Active Solar Collectors and Their Applications“, (Oxford University Press, 1985), pp. 177-178